Article

Tunable correlated states and spin-polarized phases in twisted bilayer–bilayer graphene

https://doi.org/10.1038/s41586-020-2260-6

Received: 24 March 2019

Accepted: 12 February 2020

Published online: 06 May 2020

Check for updates

Yuan Cao[1]✉, Daniel Rodan-Legrain[1], Oriol Rubies-Bigorda[1], Jeong Min Park[1], Kenji Watanabe[2], Takashi Taniguchi[2] & Pablo Jarillo-Herrero[2]✉

The recent discovery of correlated insulator states and superconductivity in magic-angle twisted bilayer graphene[1,2] has enabled the experimental investigation of electronic correlations in tunable flat-band systems realized in twisted van der Waals heterostructures[3–6]. This novel twist angle degree of freedom and control should be generalizable to other two-dimensional systems, which may exhibit similar correlated physics behaviour, and could enable techniques to tune and control the strength of electron–electron interactions. Here we report a highly tunable correlated system based on small-angle twisted bilayer–bilayer graphene (TBBG), consisting of two rotated sheets of Bernal-stacked bilayer graphene. We find that TBBG exhibits a rich phase diagram, with tunable correlated insulator states that are highly sensitive to both the twist angle and the application of an electric displacement field, the latter reflecting the inherent polarizability of Bernal-stacked bilayer graphene[7,8]. The correlated insulator states can be switched on and off by the displacement field at all integer electron fillings of the moiré unit cell. The response of these correlated states to magnetic fields suggests evidence of spin-polarized ground states, in stark contrast to magic-angle twisted bilayer graphene. Furthermore, in the regime of lower twist angles, TBBG shows multiple sets of flat bands near charge neutrality, resulting in numerous correlated states corresponding to half-filling of each of these flat bands, all of which are tunable by the displacement field as well. Our results could enable the exploration of twist-angle- and electric-field-controlled correlated phases of matter in multi-flat-band twisted superlattices.

Electronic correlations play a fundamental role in condensed-matter systems where the bandwidth is comparable to or less than the Coulomb energy between electrons. These correlation effects often manifest themselves as intriguing quantum phases of matter, such as ferromagnetism, superconductivity, Mott insulators or fractional quantum Hall states. Understanding, predicting and characterizing these correlated phases is of great interest in modern condensed-matter physics research and pose challenges to both experimentalists and theorists. Recent studies of twisted graphene superlattices have provided us with an ideal tunable platform to investigate electronic correlations in two dimensions[1,2,9–11]. Tuning the twist angle of two-dimensional (2D) van der Waals heterostructures to realize novel electronic states, an emerging field referred to as 'twistronics', has enabled physicists to explore a variety of novel phenomena[12–16]. When two layers of graphene are twisted by a specific angle, the phase diagram in the system exhibits correlated insulator states with similarities to Mott insulator systems[1,17], as well as unconventional superconducting states upon charge doping[2,9,11,18]. These effects might be originating from the many-body interactions between the electrons, when the band structure becomes substantially narrow as the twist angle approaches the first magic angle $\theta = 1.1°$ (refs. [3–5]).

Here we extend the twistronics research on graphene superlattices to a novel system with electrical displacement field tunability—twisted bilayer–bilayer graphene (TBBG), which consists of two sheets of untwisted Bernal-stacked bilayer graphene stacked together at an angle θ, as illustrated in Fig. 1a. The band structure of bilayer graphene is highly sensitive to the applied perpendicular electric displacement field[7,19,20], and therefore provides us with an extra knob to control the relative strength of electronic correlations in the bands[17]. Similar to twisted bilayer graphene (TBG)[3–5], the band structure of TBBG is flattened near about 1.1° (Fig. 2e–g)[21]. For devices with a twist angle near this value, our experiments show that the correlated insulator behaviour at $n_s/2$, $n_s/4$ and $3n_s/4$ can be sensitively turned on and off by the displacement field, where n_s is the density corresponding to fully filling one spin- and valley-degenerate superlattice band[22,23]. From their response to magnetic fields, all of these correlated states probably have a spin-polarized nature, with the $n_s/2$ state having a g-factor of about 1.5 for parallel fields, close to the bare electron spin g-factor of 2. In contrast, devices with a smaller twist angle of 0.84° show multiple displacement-field-tunable correlated states at higher fillings, consistent with the presence of several sets of correlated flat bands in the electronic structure. The combination of twist angle, electric displacement field and magnetic field provides a rich arena to investigate novel correlated phenomena in the emerging field of twistronics.

[1]Department of Physics, Massachusetts Institute of Technology, Cambridge, MA, USA. [2]National Institute for Materials Science, Tsukuba, Japan. ✉e-mail: caoyuan@mit.edu; pjarillo@mit.edu

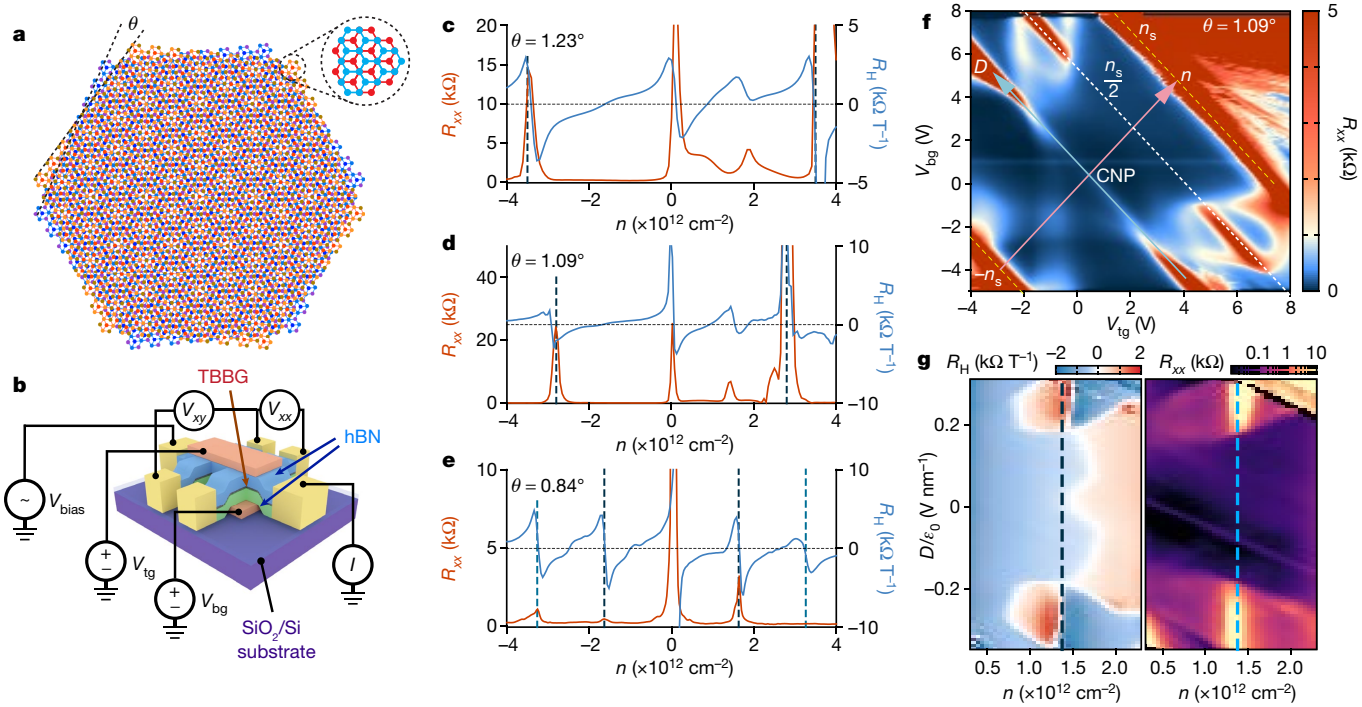

Fig. 1 | Structure and transport characterization of TBBG. a, TBBG consists of two sheets of Bernal-stacked bilayer graphene twisted at an angle θ. **b**, Schematic of a typical TBBG device with top and bottom gates and a Hall-bar geometry for transport measurements. **c**–**e**, Measured longitudinal resistance $R_{xx} = V_{xx}/I$ and low-field Hall coefficient $R_H = \mathrm{d}/\mathrm{d}B(V_{xy}/I)$ as functions of carrier density n in three devices with twist angles $\theta = 1.23°$ (**c**), 1.09° (**d**) and 0.84° (**e**). The vertical dashed lines denote multiples of the superlattice density n_s, where the peaking of R_{xx} and sign changing of R_H indicate the Fermi energy crosses a band edge of the superlattice bands. **f**, Resistance of the 1.09° TBBG device versus both V_{tg} and V_{bg}. The charge density n and displacement field D are related to the gate voltages by a linear transformation (Methods). The superlattice densities $\pm n_s$ and the half-filling at $n_s/2$ are indicated by dashed lines parallel to the D axis. Correlated insulator states are observed at $n_s/2$ filling in finite displacement fields. CNP, charge neutrality point. **g**, Map of low-field Hall coefficient R_H (left) and resistance R_{xx} (right) near the $n_s/2$ correlated states for the 1.09° TBBG device (the vertical dashed lines indicate $n_s/2$). We find that accompanying the onset of the correlated insulator states at $D/\varepsilon_0 \approx \pm 0.18$ V nm^{-1}, a new sign change of the Hall coefficient also emerges.

We fabricated high-mobility dual-gated TBBG devices with the previously reported 'tear and stack' method[22,23], using exfoliated Bernal-stacked bilayer graphene instead of monolayer graphene. The devices presumably have an AB–AB stacking configuration where the top and bottom bilayers retain the same AB stacking order, in contrast to the AB–BA structure that was predicted to show topological effects[24]. We measured the transport properties of six small-angle devices, and here we focus on three of the devices with twist angles $\theta = 1.23°$, 1.09° and 0.84° (see Extended Data Fig. 1 for other devices). The samples are all of high quality, as evident in the Landau fan diagrams, with Hall mobilities that can exceed 100,000 cm^2 V^{-1} s^{-1}, shown in Extended Data Fig. 2. Figure 1c–e shows the longitudinal resistance R_{xx} and the low-field Hall coefficient $R_H = \mathrm{d}R_{xy}/\mathrm{d}B$ versus charge density for these three devices at a temperature of $T = 4$ K, where B is the magnetic field perpendicular to the sample. In a superlattice, the electronic band structure is folded in the mini-Brillouin zone, defined by the moiré periodicity[4]. Each band in the mini-Brillouin zone can accommodate a total charge density of $n_s = 4/A$, where A is the size of the moiré unit cell and the pre-factor accounts for the spin and valley degeneracies[4,21,22]. The experimental results show a sign change in the Hall coefficient R_H at each multiple of n_s (vertical dashed lines in Fig. 1c–e), indicating the switching of hole-like pockets to electron-like pockets, and peaks in R_{xx}, indicating the crossing of new band edges (for $\theta = 0.84°$, the band edges at $-n_s$ and $\pm 2n_s$ may have only small gaps or may even be semi-metallic, and hence do not exhibit prominent peaks in R_{xx}). The sharpness of the peaks confirms that the devices exhibit relatively low disorder and have well-defined twist angles.

In the $\theta = 1.23°$ and $\theta = 1.09°$ devices, we observe signatures of newly formed gaps at $n_s/2$ when a displacement field D is applied perpendicular to the device. The dual-gate device geometry allows us to independently vary the total charge density n and D (see Methods for details of the transformation between gate voltages and (n, D)). Figure 1f shows the resistance map in the top gate voltage–bottom gate voltage (V_{tg}–V_{bg}) space for the $\theta = 1.09°$ device. At $D = 0$, no insulating behaviour other than the full-filling gaps at $\pm n_s$ is observed. However, when a displacement field D is applied in either direction, an insulating state appears at $n_s/2$ for a range of $|D|$. This new insulating state induced by the displacement field is further examined by measuring the Hall coefficient R_H versus n and D, as shown in the left panel of Fig. 1g ($\theta = 1.09°$ device), and comparing with R_{xx} shown in the right panel. At the onset of the insulating states at $D/\varepsilon_0 \approx \pm 0.18$ V nm^{-1}, where ε_0 is the vacuum permittivity, R_H develops additional sign changes adjacent to the insulating states, suggesting the creation of new gaps by the displacement field. The insulating states disappear when D/ε_0 exceeds ±0.35 V nm^{-1}. In both the $\theta = 1.09°$ device and the $\theta = 1.23°$ devices, we find signatures of the onset of correlated behaviour at $n = -n_s/2$ and $D = 0$, but no well-developed insulating state is observed (Extended Data Fig. 1, Methods).

In the $\theta = 1.23°$ device, we observe a similar but more intricate hierarchy of tunable insulating states that stem from the interplay of correlations, the superlattice bands and the magnetic field. Figure 2a shows the n–D resistance map for the $\theta = 1.23°$ TBBG device measured at $T = 0.07$ K. Noticeably, as $|D|$ is increased, the insulating state at charge neutrality $n = 0$ strengthens in the same way as in the Bernal-stacked bilayer graphene[7,19,20], while the superlattice gaps at $\pm n_s$ weaken and eventually disappear (at $|D|/\varepsilon_0 > 0.6$ V nm^{-1} for the $+n_s$ insulating state and at $|D|/\varepsilon_0 > 0.35$ V nm^{-1} for the $-n_s$ insulating state). The band structures of TBBG in zero and finite external displacement fields calculated using

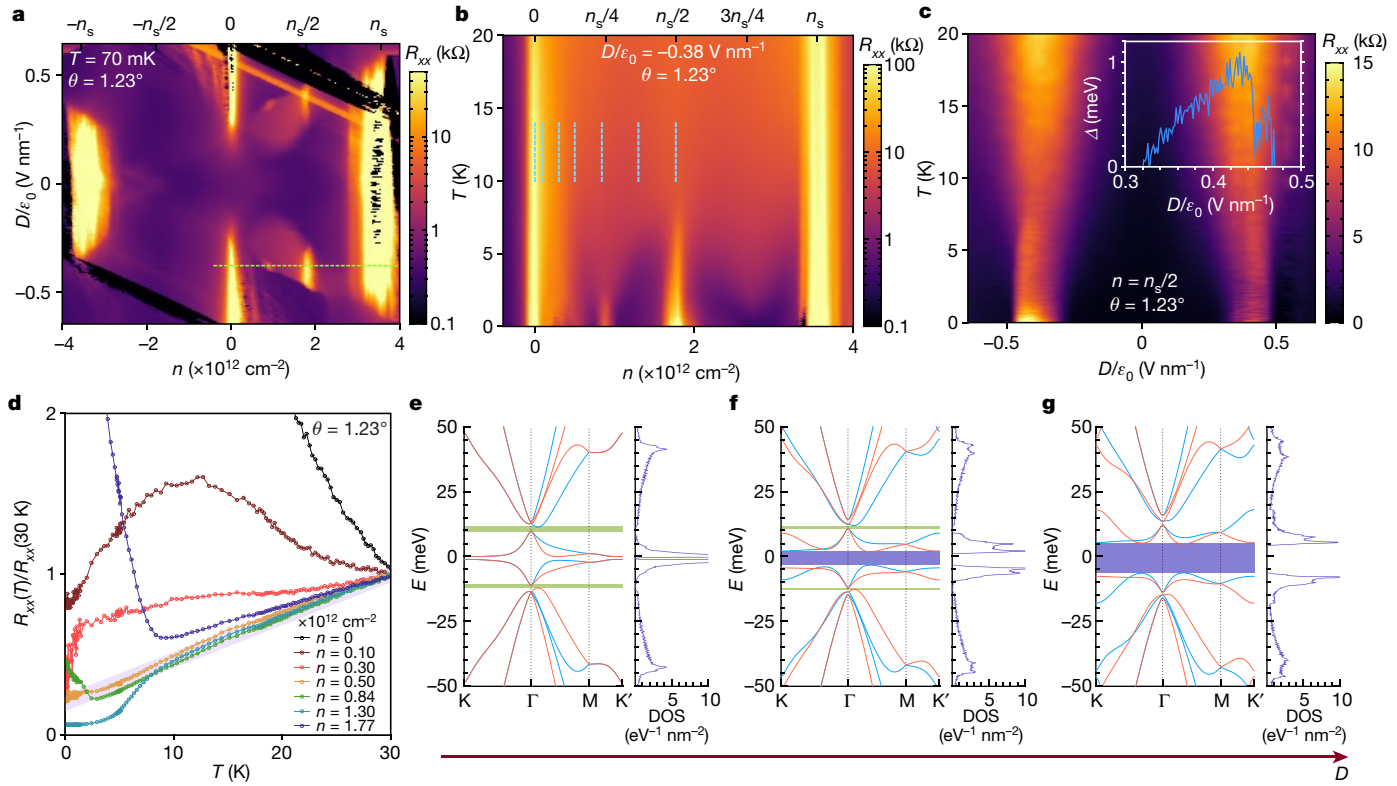

Fig. 2 | Displacement-field-tunable correlated insulator states in TBBG. **a**, Colour plot of resistance versus charge density n and displacement field D ($\theta = 1.23°$ device, section 1, see Methods). The green dashed line cutting through the $D < 0$ correlated state is the linecut along which **b** is taken (for the $\theta = 1.23°$ device, section 2, see Methods). **b**, Resistance versus n and T at a fixed $D/\varepsilon_0 = -0.38$ V nm^{-1}. The correlated insulator states at $n_s/4$ and $n_s/2$ are suppressed by increasing the temperature. **c**, Resistance at density $n_s/2$ versus displacement field and temperature. The resistance shows a maximum at approximately $D/\varepsilon_0 = \pm 0.4$ V nm^{-1}, the region where the correlated insulator state is present. The inset shows the thermal activation gap extracted from temperature dependence at different values of D across the $n_s/2$ state. **d**, Normalized resistance curves versus temperature at various densities between 0 and $n_s/2 \approx 1.77 \times 10^{12}$ cm^{-2}, which are indicated by dashed lines in **b**. Away from the charge neutrality point, all resistance curves show approximately linear R–T behaviour above 10 K, with similar slopes (Extended Data Fig. 3). **e**–**g**, Calculated band structure (left) and density of states (DOS; right) for $\theta = 1.23°$ TBBG at $\Delta V = 0$ (**e**), $\Delta V = 6$ mV (**f**) and $\Delta V = 12$ mV (**g**), where ΔV is the potential difference between adjacent graphene layers induced by the external displacement field (assumed to be the same between all layers). Single-particle bandgaps in the dispersion are highlighted green (below and above the flat bands) and purple (at charge neutrality) bars.

a continuum approximation are shown in Fig. 2e–g (see Methods for details). It should be noted that, although TBBG has twice the number of graphene layers than TBG, the band counting is the same, that is, each band (spin and valley degenerate) accommodates four electrons per moiré unit cell. At zero displacement field, the calculated gap at the charge neutrality is negligible, while the superlattice gaps above and below the flat bands are non-zero. When the displacement field is increased, the charge neutrality gap quickly widens while the superlattice gaps become smaller and eventually vanish, in agreement with our experimental observations.

At intermediate displacement fields around $D/\varepsilon_0 = -0.38$ V nm^{-1}, we observe the insulating states not only at $n_s/2$ over a wider range of D, but also at $n_s/4$ over a smaller range (Fig. 2a). We attribute these states to a Mott-like mechanism similar to those observed in TBG, which results from the Coulomb repulsion of the electrons in the flat bands when each unit cell hosts exactly one or two electrons, corresponding to $n_s/4$ and $n_s/2$ fillings, respectively. The $n_s/4$ state requires a finer tuning of D to be revealed, possibly due to the smaller gap size. This is evident from Fig. 2b, where we show the resistance versus n and temperature T with the displacement field D/ε_0 fixed at −0.38 V nm^{-1}. While the $n_s/2$ state persists up to approximately 8 K, the $n_s/4$ state disappears at less than 3 K, indicating a smaller gap. Figure 2c shows the resistance of the $n_s/2$ state versus the displacement field and temperature. The 'optimal' displacement field to reach the maximal resistance is approximately ±0.4 V nm^{-1}. As the temperature increases, the peak in R_{xx} not only decreases in value but also broadens in D. In the inset, we show the evolution of the gap versus the displacement field. At temperatures higher than 10 K and away from the charge neutrality point, the transport is dominated by a linear R–T behaviour similar to that observed in TBG (Fig. 2d, see also Extended Data Fig. 3, Methods)[2,9,25,26].

Figure 3 shows the response of the various correlated states to magnetic fields in the perpendicular or in-plane direction with respect to the sample plane. Figure 3a–c shows the n–D maps of the resistance for the $\theta = 1.23°$ device at $B = 0$ T, $B_\perp = 8$ T and $B_\parallel = 8$ T, respectively. The plots focus on densities from $n = 0$ to $n = n_s$. Figure 3a shows the band insulator states at $n = 0$ and $n = n_s$, as well as the correlated insulating states at $n_s/2$ and $n_s/4$ (encircled by dashed lines), but not at $3n_s/4$ filling at this zero magnetic field. Interestingly, at $B_\perp = 8$ T (Fig. 3b), the correlated insulating states at $n_s/4$ and $n_s/2$ vanish at their original positions centred around $D/\varepsilon_0 = -0.38$ V nm^{-1}, whereas new insulating states appear at $n = n_s/4$, $D/\varepsilon_0 \approx -0.2$ to -0.35 V nm^{-1}, and $n = n_s/2$, $D/\varepsilon_0 \approx -0.45$ to -0.6 V nm^{-1}, above and below their original positions at $B = 0$, respectively. A new correlated insulating state also now appears at $3n_s/4$, $D/\varepsilon_0 \approx -0.4$ to -0.5 V nm^{-1}. However, no such strong shift is observed with in-plane magnetic field (Fig. 3c). At $B_\parallel = 8$ T, the correlated insulating states are clearly visible at all integer electron fillings ($n_s/4$, $n_s/2$, $3n_s/4$) near $D/\varepsilon_0 = -0.38$ V nm^{-1}. Figure 3d, e shows the evolution of the $n_s/2$ insulating state as a function of $B_\perp$ and $B_\parallel$. An abrupt

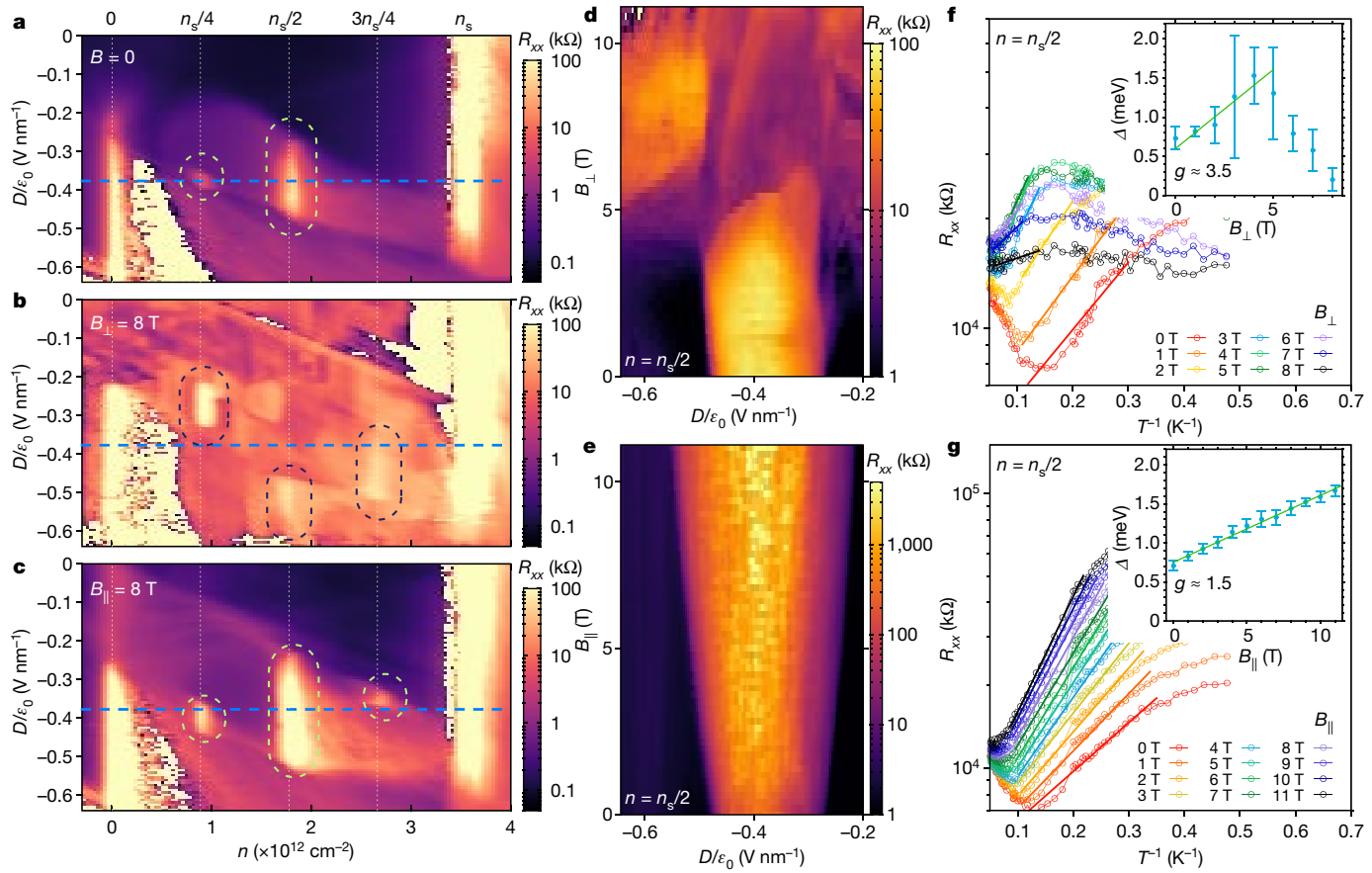

Fig. 3 | Magnetic field response of the displacement-field-tunable correlated insulator states in TBBG. a–**c**, Resistance plot for the $\theta = 1.23°$ TBBG device in magnetic fields of $B = 0$ (**a**), $B_\perp = 8$ T perpendicular to the sample (**b**) and $B_\parallel = 8$ T parallel to the sample (**c**). All measurements are taken at sample temperature $T = 0.07$ K. Various correlated states at integer electron fillings of the moiré unit cell are indicated by dashed circles. At zero field, only the $n_s/4$ and $n_s/2$ states appear around $|D|/\varepsilon_0 = 0.38$ V nm^{-1} (denoted by blue dashed lines). In a perpendicular field of 8 T, the $n_s/4$ state shifts towards lower $|D|$, the $n_s/2$ state shifts towards higher $|D|$ and a $3n_s/4$ state also emerges. In a parallel field of 8 T, however, the position of the states barely shifts but their resistance increases monotonically. **d**, **e**, Resistance at $n = n_s/2$ versus displacement field and magnetic field applied perpendicular (**d**) and in-plane (**e**) with respect to the device. While the correlated insulator state monotonically strengthens in $B_\parallel$, the perpendicular field induces a phase transition at around $B_\perp = 5$ T, where the correlated state abruptly shifts to higher $|D|$. **f**, **g**, Temperature dependence of the resistance at the $n_s/2$ insulator in perpendicular (**f**) and in-plane (**g**) magnetic fields. The insets show the thermal activation gaps extracted from the Arrhenius fits ($R \approx e^{\frac{\Delta}{2k_B T}}$, where k_B is the Boltzmann constant) in the main figures (solid lines) versus the magnitude of the field in the respective orientation. Error bars correspond to a confidence level of 0.99. The linear fit of the thermal activation gap gives a g-factor of about 3.5 for the perpendicular field (up to 5 T only) and 1.5 for the in-plane field (entire field range).

shift in the range of D for which the insulating state appears occurs at $B_\perp = 5$ T, whereas the insulating state strengthens monotonically with the in-plane magnetic field.

The key difference between the effects of the perpendicular and in-plane magnetic fields lies in the fact that the lateral dimension of the unit cell in TBBG, about 10 nm, is much larger than the thickness of the system, about 1 nm. Therefore, while both fields couple equally to the spins of the correlated electrons, $B_\parallel$ has a much weaker (but non-zero) effect on the orbital movement of the electrons. To theoretically understand the behaviour of the correlated insulating states in a magnetic field, we first have to identify their ground state. Figure 3f, g shows the evolution of the thermal activation gap of the $n_s/2$ state in both $B_\perp$ and $B_\parallel$. We find a g-factor of $g_\perp \approx 3.5$ for the perpendicular direction (up to 5 T before the shift occurs) and a g-factor of $g_\parallel \approx 1.5$ for the in-plane direction. $g_\parallel$ is close to (but less than) $g = 2$, which is expected for a spin-polarized ground state with contribution from only the electron spins. This difference is theoretically expected because of finite in-plane orbital effects[27]. Therefore, on the basis of these measurements, we may conclude that the correlated insulating states have a spin-polarized nature. These observations establish TBBG as a distinctive system from the previously reported magic-angle TBG system[1,2,9], which exhibits half-filling insulating states that are shown to be spin unpolarized, as they are suppressed by an in-plane magnetic field. In $B_\perp$, however, one would expect orbital effects to have a more substantial role. We may attribute the larger $g_\perp$ of about 3.5 to exchange-induced enhancement effects, similar to what is observed in Landau levels of gallium arsenide quantum wells and graphene[28,29]. In Extended Data Fig. 4, we provide additional magnetic field response data for the $n_s/4$ and the $3n_s/4$ states. Both of these states also exhibit a spin-polarized behaviour, as they become more resistive under the in-plane magnetic field.

In addition to the discussion above, we noticed that all the correlated insulating states in the $\theta = 1.23°$ TBBG device, whether at zero magnetic field or high magnetic fields, lie within the range $D/\varepsilon_0 \approx -0.6$ to -0.2 V nm^{-1}. Coincidentally, this is also the range where both the gap at the charge neutrality ($n = 0$) and the gap at the superlattice density ($n = n_s$) are well developed (that is, the case in Fig. 2f). On the basis of this observation, we suggest that the displacement field tunability of the correlated states is tied to the modulation of the single-particle bandgaps by the displacement field[27]. When either gap at $n = 0$ or $n = n_s$ is absent, the thermally excited or disorder-scattered carriers from the upper or lower bands would suppress the ordering of the electrons and hence the correlated states. Further theoretical

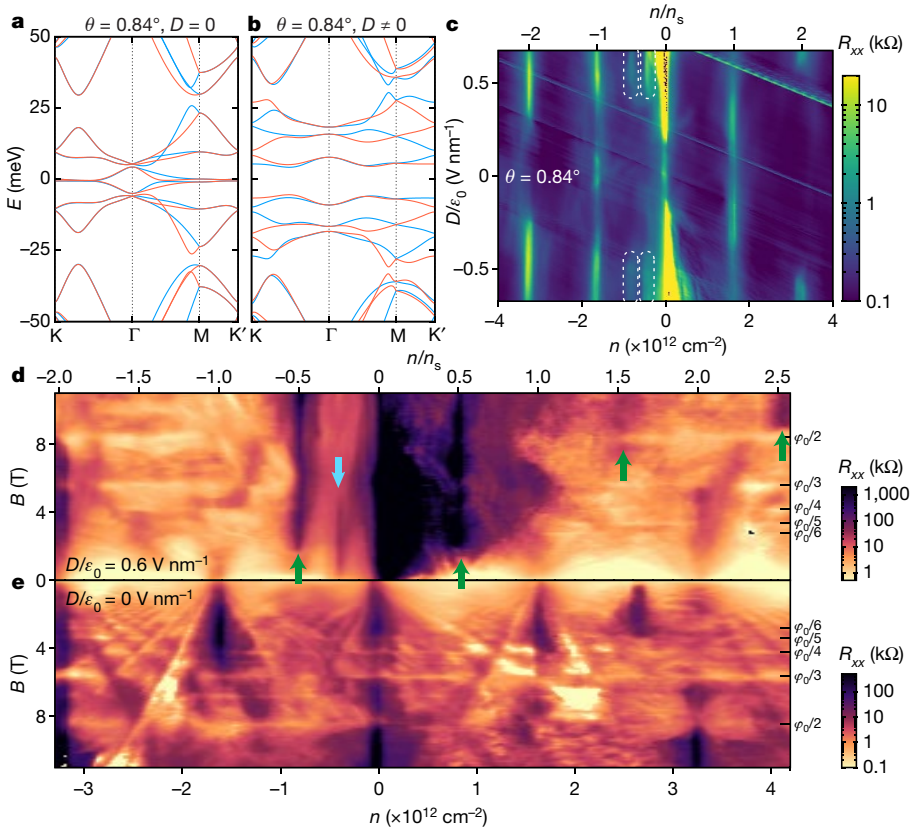

Fig. 4 | Correlated insulator states in a multi-flat-band system. **a**, **b**, Calculated band structure of $\theta = 0.84°$ TBBG without an interlayer potential (**a**) and with an interlayer potential $\Delta V = 18$ mV (**b**). Near charge neutrality, within a 50-meV window, there are in total six sets of flat bands spanning densities $-3n_s$ to $3n_s$. Upon applying a displacement field, these bands are further flattened and separated from each other, which makes them more prone to giving rise to correlated states at each half-filling. **c**, Resistance map of a $\theta = 0.84°$ TBBG device measured at $T = 0.07$ K. The top axis is the charge density normalized to the superlattice density n_s. Besides the D-tunable gaps at multiples of n_s, we find signatures of correlated states at $n/n_s = -1/2, -1/4$ for $|D|/\varepsilon_0 > 0.4$ V nm^{-1}, which are indicated by dashed circles. **d**, Resistance as a function of charge density and perpendicular magnetic field B when a displacement is present, $D/\varepsilon_0 = 0.6$ V nm^{-1}. We find clear correlated states at $n/n_s = -1/2, 1/4$ and $1/2$, and also evidences at 3/2 and 5/2 fillings, as indicated by arrows (blue and green arrows indicate half-fillings and quarter-filling, respectively). **e**, For comparison, when no displacement field is present, we do not find any signature of half-filling correlated states. Owing to the formation of a superlattice, we also observe Hofstadter butterfly related features when B is such that the magnetic flux in each unit cell is equal to $\varphi_0/2, \varphi_0/3, \varphi_0/4$ and so on, where $\varphi_0 = h/e$ is the flux quantum, h and e being Planck's constant and electron charge, respectively.

work is needed to reveal the detailed structure of the displacement field dependence of the correlated states.

We have also investigated the regime of substantially smaller twist angles. Unlike the case of TBG, further reduction of the twist angle of TBBG to 0.84° results not in one, but rather three pairs of flat bands, separated from other bands by bandgaps (Fig. 4a). The application of an electrical displacement field further flattens these bands and separates them from each other (Fig. 4b). This would imply that all electrons within the density range $-3n_s$ to $+3n_s$ might experience strong Coulomb interactions and that their correlations can get further enhanced by applying a displacement field. These predictions from the band theory are consistent with our experimental observations. In Fig. 4c, where we show the resistance map of the $\theta = 0.84°$ TBBG device versus n and D, we indeed find that the weak signatures of the $-n_s/2$ and $-n_s/4$ correlated insulating states appear only at high displacement fields $|D|/\varepsilon_0 > 0.4$ V m^{-1} (encircled by white dashed lines). The full-filling gaps at $\pm n_s$ and $\pm 2n_s$ are tunable by the displacement field to different extents as well.

As we turn on a perpendicular magnetic field, a series of correlated insulator states appear across the entire density range spanning the multiple flat bands. Figure 4d, e shows the Landau fan diagrams at $D/\varepsilon_0 = 0.6$ V m^{-1} and $D = 0$, respectively. At zero displacement field, the Landau fan shows a complicated Hofstadter butterfly pattern due to commensurate flux threading into the unit cell[12–14] (see also Methods, Extended Data Fig. 2), but no correlated state is observed at half-fillings or quarter-fillings. We note that a resistive region appears at $n \approx 1.63n_s$ in Fig. 4e, which does not coincide with any commensurate filling and might be ascribed to twist-angle inhomogeneity in the sample. In contrast, at $D/\varepsilon_0 = 0.6$ V nm^{-1}, we find clear signatures of correlated states at $n_s/2$ and $-n_s/2$ in the centre flat bands, and weak evidences at $3n_s/2$ and $5n_s/2$ in the upper flat bands. All of these half-filling correlated states appear to be enhanced by the application of a perpendicular magnetic field, which we attribute to the same spin/orbital combined enhancement of the correlated gaps as in the $n_s/2$ state of the $\theta = 1.23°$ device (Fig. 3f). The correlated states at $\pm n_s/2$ appear to be much stronger than the states at $3n_s/2$ and $5n_s/2$ in high magnetic fields, consistent with the fact that from our calculations, the pair of bands closer to charge neutrality is much flatter than the other two pairs farther away from charge neutrality, as can be seen in Fig. 4b. The resistance of the quarter-filling state at $n_s/4$, however, does not increase monotonically with the perpendicular field, but rather eventually gets suppressed at 5 T.

Our results show that TBBG exhibits a rich spectrum of correlated phases tunable by twist angle, electric displacement field and magnetic field, enabling further studies of strongly correlated physics and topology in multi-flat-band systems[21].

Online content

Any methods, additional references, Nature Research reporting summaries, source data, extended data, supplementary information, acknowledgements, peer review information; details of author contributions and competing interests; and statements of data and code availability are available at https://doi.org/10.1038/s41586-020-2260-6.

1. Cao, Y. et al. Correlated insulator behaviour at half-filling in magic-angle graphene superlattices. *Nature* **556**, 80–84 (2018).
2. Cao, Y. et al. Unconventional superconductivity in magic-angle graphene superlattices. *Nature* **556**, 43–50 (2018).
3. Suárez Morell, E., Correa, J. D., Vargas, P., Pacheco, M. & Barticevic, Z. Flat bands in slightly twisted bilayer graphene: tight-binding calculations. *Phys. Rev. B* **82**, 121407 (2010).
4. Bistritzer, R. & MacDonald, A. H. Moiré bands in twisted double-layer graphene. *Proc. Natl Acad. Sci. USA* **108**, 12233–12237 (2011).
5. Lopes dos Santos, J. M. B., Peres, N. M. R. & Castro Neto, A. H. Continuum model of the twisted graphene bilayer. *Phys. Rev. B* **86**, 155449 (2012).
6. Carr, S. et al. Twistronics: manipulating the electronic properties of two-dimensional layered structures through their twist angle. *Phys. Rev. B* **95**, 075420 (2017).
7. McCann, E. & Koshino, M. The electronic properties of bilayer graphene. *Rep. Prog. Phys.* **76**, 056503 (2013).
8. Castro Neto, A. H., Guinea, F., Peres, N. M. R., Novoselov, K. S. & Geim, A. K. The electronic properties of graphene. *Rev. Mod. Phys.* **81**, 109–162 (2009).
9. Yankowitz, M. et al. Tuning superconductivity in twisted bilayer graphene. *Science* **363**, 1059–1064 (2019).
10. Sharpe, A. L. et al. Emergent ferromagnetism near three-quarters filling in twisted bilayer graphene. *Science* **365**, 605–608 (2019).
11. Lu, X. et al. Superconductors, orbital magnets and correlated states in magic-angle bilayer graphene. *Nature* **574**, 653–657 (2019).
12. Hunt, B. et al. Massive Dirac fermions and Hofstadter butterfly in a van der Waals heterostructure. *Science* **340**, 1427–1430 (2013).
13. Ponomarenko, L. A. et al. Cloning of Dirac fermions in graphene superlattices. *Nature* **497**, 594–597 (2013).
14. Dean, C. R. et al. Hofstadter's butterfly and the fractal quantum Hall effect in moiré superlattices. *Nature* **497**, 598–602 (2013).
15. Krishna Kumar, R. et al. High-temperature quantum oscillations caused by recurring Bloch states in graphene superlattices. *Science* **357**, 181–184 (2017).
16. Li, G. et al. Observation of Van Hove singularities in twisted graphene layers. *Nat. Phys.* **6**, 109–113 (2010).
17. Chen, G. et al. Evidence of a gate-tunable Mott insulator in a trilayer graphene moiré superlattice. *Nat. Phys.* **15**, 237–241 (2019).
18. Chen, G. et al. Signatures of tunable superconductivity in a trilayer graphene moiré superlattice. *Nature* **572**, 215–219 (2019).
19. Oostinga, J. B., Heersche, H. B., Liu, X., Morpurgo, A. F. & Vandersypen, L. M. K. Gate-induced insulating state in bilayer graphene devices. *Nat. Mater.* **7**, 151–157 (2008).
20. Zhang, Y. et al. Direct observation of a widely tunable bandgap in bilayer graphene. *Nature* **459**, 820–823 (2009).
21. Zhang, Y.-H., Mao, D., Cao, Y., Jarillo-Herrero, P. & Senthil, T. Nearly flat Chern bands in moiré superlattices. *Phys. Rev. B* **99**, 075127 (2019).
22. Cao, Y. et al. Superlattice-induced insulating states and valley-protected orbits in twisted bilayer graphene. *Phys. Rev. Lett.* **117**, 116804 (2016).
23. Kim, Y. et al. Charge inversion and topological phase transition at a twist angle induced Van Hove singularity of bilayer graphene. *Nano Lett.* **16**, 5053–5059 (2016).
24. Koshino, M. Band structure and topological property of twisted double bilayer graphenes. *Phys. Rev. B* **99**, 235406 (2019).
25. Polshyn, H. et al. Large linear-in-temperature resistivity in twisted bilayer graphene. *Nat. Phys.* **15**, 1011–1016 (2019).
26. Cao, Y. et al. Strange metal in magic-angle graphene with near Planckian dissipation. *Phys. Rev. Lett.* **124**, 076801 (2020).
27. Lee, J. Y. et al. Theory of correlated insulating behaviour and spin-triplet superconductivity in twisted double bilayer graphene. *Nat. Commun.* **10**, 5333 (2019).
28. Raymond, A. et al. Gigantic exchange enhancement of spin *g*-factor for two-dimensional electron gas in GaAs. *Solid State Commun.* **55**, 271–274 (1985).
29. Young, A. F. et al. Spin and valley quantum Hall ferromagnetism in graphene. *Nat. Phys.* **8**, 550–556 (2012).

Publisher's note Springer Nature remains neutral with regard to jurisdictional claims in published maps and institutional affiliations.

© The Author(s), under exclusive licence to Springer Nature Limited 2020

Methods

Fabrication and measurement

The reported devices were fabricated with two sheets of Bernal-stacked bilayer graphene and encapsulated by two hexagonal boron nitride (hBN) flakes. Both bilayer graphene and hBN were exfoliated on SiO_2/Si substrates, and the thickness and quality of the flakes were confirmed with optical microscopy and atomic force microscopy. A modified polymer-based dry pick-up technique was used for the fabrication of the heterostructures. A poly(bisphenol A carbonate) (PC)/polydimethylsiloxane (PDMS) layer on a glass slide was positioned in the micro-positioning stage to first pick up an hBN flake at around 100 °C. The van der Waals interaction between the hBN and bilayer graphene then allowed us to tear the bilayer graphene flake, which was then rotated at a desired angle and stacked at room temperature. The resulting hBN/bilayer graphene/bilayer graphene heterostructure was released on another hBN flake on a palladium/gold back gate that was pre-heated to 170 °C, using a hot-transfer method[30,31]. The desired geometry of the devices was achieved with electron beam lithography and reactive ion etching. The electrical contacts and top gate were deposited by thermal evaporation of chromium/gold, making edge contacts to the encapsulated graphene[32].

Electronic transport measurements were performed in a dilution refrigerator with a superconducting magnet, with a base electronic temperature of 70 mK. The data were obtained with low-frequency lock-in techniques. We measured the current through the sample amplified by 10^7 V A^{-1} and the four-probe voltage amplified by 1,000, using SR-830 lock-in amplifiers that were all synchronized to the same frequency between around 1 and 20 Hz. For resistance measurements, we typically used a voltage excitation of less than 100 μV or current excitation of less than 10 nA.

List of measured TBBG devices

Following the definition given in the main text and accounting for offsets in the gate voltages due to impurity doping, n and D are related to the top and bottom gate voltages V_{tg} and V_{bg} by

$$n = [c_{tg}(V_{tg} - V_{tg,0}) + c_{bg}(V_{bg} - V_{bg,0})]/e$$

$$D = [-c_{tg}(V_{tg} - V_{tg,0}) + c_{bg}(V_{bg} - V_{bg,0})]/2$$

Extended Data Table 1 lists the twist angles and parameters c_{tg} (top gate capacitance per area), c_{bg} (bottom gate capacitance per area), $V_{tg,0}$ (top gate voltage offset), $V_{bg,0}$ (bottom gate voltage offset) and n_s (superlattice density) for all devices discussed in this work, including those shown in the Extended Data figures. e is unit electron charge. These parameters are estimated to satisfy that all diagonal features in the V_{tg}–V_{bg} maps are rotated to be vertical in the corresponding n–D maps, and the features should be symmetrical with respect to $D = 0$ after the transformation.

In Extended Data Fig. 1a–f, we show V_{tg}–V_{bg} resistance maps for all six TBBG devices we measured. Extended Data Fig. 1c, d was measured in the same TBBG sample, but in different sample regions that are approximately 27 μm apart (sections 1 and 2, respectively). Both regions have identical parameters (hence the two identical rows in Extended Data Table 1), with the same twist angle $\theta = 1.23°$, and also nearly identical transport characteristics. The two sections are electrically disconnected via etching, but the extracted twist angles from the data have a difference of less than 0.01°, suggesting very uniform twist angles across this entire sample.

In almost all TBBG samples, we noticed a peculiar cross-like pattern around $(n, D) = (-n_s/2, 0)$, that is, near p-side half-filling of the superlattice band. This is especially apparent in the 1.09° and 1.23° devices, which are highlighted in Extended Data Fig. 1g, h. The p-side band does not exhibit a strong D-tunable correlated state as elaborated in the main text, possibly due to the larger bandwidth compared with its n-side counterpart. This cross-like pattern might represent an onset of correlated behaviour near half-filling of the band. Further experimental work and theoretical insight are needed to understand this phenomenon.

Sample quality and Landau fans

To demonstrate the high quality of our fabricated TBBG devices, we measured the Landau fan diagrams and Hall mobilities of all three devices discussed in the main text, as shown in Extended Data Fig. 2. The Hall mobilities are extracted from the ratio between the Hall coefficient R_H and longitudinal resistance at small magnetic fields ($B < 0.5$ T). All three samples exhibit high Hall mobilities close to or above 100,000 $cm^2 V^{-1} s^{-1}$.

All three devices also show clear Landau fans starting from about 1 T. The filling factor of each level is labelled in the lower panels of each plot. In particular, due to the lower angle of the $\theta = 0.84°$ device, its Landau fan displays a complicated Hofstadter's butterfly pattern starting from 3 T.

Linear R–T behaviour

Extended Data Fig. 3 shows the resistance versus temperature behaviour, at different densities, observed across several small-angle TBBG devices. In the 1.23° device, we find approximately linear R–T behaviour above 10 K for densities ranging from around 0.5×10^{12} to 2.5×10^{12} cm^{-2}, encompassing the $n_s/2$ correlated state. The resistance slope in this range of densities does not vary very substantially, ranging from around 210 to 350 Ω K^{-1}. As all our devices have length-to-width ratios close to one, these slope values are therefore close to those reported in TBG[25,26]. In stark contrast, the resistance behaviour in the hole-doping side ($n < 0$), as shown in Extended Data Fig. 3b, shows qualitatively different behaviour: it does not show linear R–T characteristics, at least up to 30 K, and the resistance value is about an order of magnitude smaller than on the electron-doping side. These data are consistent with the picture that the electron-doping band is flatter than the hole-doping band, therefore exhibiting more pronounced correlated phenomena, examples being the $n_s/2$ insulator state and the linear R–T behaviour. Extended Data Fig. 3c shows R–T curves close to the $n_s/2$ state.

The data for the 1.09° device show a similar trend of linear R–T behaviour starting around 5–10 K, as shown in Extended Data Fig. 3d.

In the 0.84° device, we find a very different behaviour. There is a region of sublinear or approximately linear R–T behaviour at all densities, except at multiples of n_s, but the resistance slope is now strongly dependent on the charge density n. The slope approximately follows a power law $\frac{dR_{xx}}{dT} \propto n^a$ where $a \approx -1.77$ (see inset).

Theoretical methods

The band structures shown in the main text are calculated using a continuum model based on the original continuum model for TBG[4,5], which qualitatively captures most of the important features of the bands in TBBG including displacement-field dependence. To the lowest order, the continuum model of twisted graphene superlattices is built on the approximation that the interlayer coupling between the A/B sublattice of one layer and the A/B sublattice of the other layer has a sinusoidal variation over the periodicity of the moiré pattern. For the three possible directions of interlayer connections between the wave vectors in the Brillouin zone, there are three connection matrices

$$H_1 = w\begin{pmatrix} 1 & 1 \\ 1 & 1 \end{pmatrix}$$

$$H_2 = w\begin{pmatrix} \omega^2 & 1 \\ \omega & \omega^2 \end{pmatrix}$$

$$H_3 = w\begin{pmatrix} \omega & 1 \\ \omega^2 & \omega \end{pmatrix}$$

where w is the interlayer hopping energy and $\omega = \exp(2\pi i/3)$. $H_{i,\alpha\beta}$, with $\alpha\beta$ = A, B represents the hopping between sublattice α in the first layer to sublattice β in the second layer, with momentum transfer determined by i (see ref. [4] for definition). Note that in this gauge choice, the origin of rotation is chosen where the B sublattice of the first layer coincides with the A sublattice of the second layer, so that the $H_{i,\mathrm{BA}}$ component has zero phase while the other terms acquire phases. A different gauge choice is equivalent to an interlayer translation, which has been shown to have a negligible effect in the case of small twist angles[4,5].

To extend this formulation to TBBG, we add a simplified bilayer graphene Hamiltonian

$$H_\mathrm{b} = \begin{pmatrix} 0 & 0 \\ w_\mathrm{b} & 0 \end{pmatrix}$$

between the non-twisted layers. The momentum transfer is zero since the bilayers are not twisted and the coupling is constant over the moiré unit cell. For simplicity, we consider only the 'dimer' coupling in the bilayer, neglecting second-nearest-neighbour hopping terms and trigonal warping terms. The two bilayers in TBBG (layers 1–2 and layers 3–4) have the same stacking order, that is, for zero twist angle the total stacking would be 'ABAB' instead of 'ABBA'. In the calculations used in the main text, we used parameters w = 0.1 eV and w_b = 0.4 eV, so that when either parameter is turned off we obtain either the two non-interacting bilayer graphene (w = 0) or the non-interacting TBG and two-monolayer graphene (w_b = 0).

Additional magnetic-field-response data

Extended Data Fig. 4 shows the response of correlated states at $n_s/4$ and $3n_s/4$ in a perpendicular or in-plane magnetic field, similar to Fig. 3d, e, for the θ = 1.23° device. For the $n_s/4$ state, we also find a signature of a phase transition at $D/\varepsilon_0 = -0.36$ V nm^{-1}, manifesting as a shift of the D location of the correlated insulator as $B_\perp$ exceeds 6 T. The $3n_s/4$ state shows an overall monotonic increase of resistance and exhibits no shift in the position in D. In an in-plane field, however, as shown in Extended Data Fig. 4b, d, both quarter-filling states show a monotonic enhancement as $B_\parallel$ is increased, suggesting that they may have a similar spin-polarized ground state as the $n_s/2$ state.

Current–voltage curves and the impact of excitation current on g-factor

In Extended Data Fig. 5, we have plotted the current–voltage (I–V) curves and differential resistance curves of the θ = 1.23° device when it is in the correlated insulator states at $n_s/4$ and $n_s/2$. In the insulator states, we find a highly nonlinear region near zero d.c. bias $I_\mathrm{b} = 0$ where the differential resistance $\mathrm{d}V_{xx}/\mathrm{d}I_\mathrm{b}$ is substantially enhanced. This is in agreement with the existence of a small energy gap, which is overcome at higher bias voltages/currents. Outside of the insulator regions (such as shown in Extended Data Fig. 5b), the I–V curves are mostly linear. For measuring the g-factors at $n_s/2$, we therefore used a much smaller excitation current of 0.1 nA to truthfully measure the differential resistance at $I_\mathrm{b} = 0$.

We comment here on the effect of the a.c. excitation current on the measured gap sizes and the g-factor. When sourcing an a.c. bias current to measure the resistance using a lock-in technique, we effectively measure a weighted average of the differential resistance near zero bias. Owing to the highly nonlinear I–V curve at the $n_s/2$ state, if the a.c. excitation is large, this average value will be much less than the peak value. Furthermore, the average value measured in this case can have a very different temperature dependence compared with the zero-bias value. For example, although to the best of our knowledge there is no detailed analysis of the high-bias behaviour in the correlated insulator state of TBG, TBBG or related systems, if one considers the high-bias transport to have a contribution from a mechanism similar to Zener breakdown in semiconductors in an electrical field, the current is essentially independent of the temperature. There could be other contributions to the high-bias transport as well, but in general their temperature dependence would not be identical to the zero-bias peak. In the Arrhenius fit that we use to extract the gap size, the gap size Δ is basically equal to how fast the resistance exponentially rises with T^{-1}. Therefore, a reduction of temperature dependence means that by averaging the higher bias differential resistance one would substantially underestimate the energy gap Δ, and also the g-factor $g \propto \delta\Delta/\delta B$.

In Extended Data Fig. 6, we compare the Arrhenius fits of the resistance at $n_s/2$ and $n_s/4$ states, using a small excitation (0.1 nA) and a larger excitation (around 5–10 nA). We indeed find that by using an excessive excitation, both the gap size Δ and the g-factor are substantially underestimated. In particular, owing to the larger nonlinearity at the $n_s/2$ state, its g-factor is underestimated by a factor of about three by using the larger excitation. Therefore, one should keep these nonlinear effects in mind when doing temperature-dependent measurements on such resistive states to obtain accurate results.

Data availability

The data that support the findings of this study are available from the corresponding authors upon reasonable request.

30. Pizzocchero, F. et al. The hot pick-up technique for batch assembly of van der Waals heterostructures. *Nat. Commun.* **7**, 11894 (2016).
31. Purdie, D. G. et al. Cleaning interfaces in layered materials heterostructures. *Nat. Commun.* **9**, 5387 (2018).
32. Wang, L. et al. One-dimensional electrical contact to a two-dimensional material. *Science* **342**, 614–617 (2013).

Acknowledgements We acknowledge discussions with S. Todadri, L. Fu, P. Kim, X. Liu, S. Fang and E. Kaxiras. This work was supported by the National Science Foundation under award DMR-1809802 (data analysis by Y.C.), the Center for Integrated Quantum Materials under NSF grant DMR-1231319 (fabrication by D.R.-L.), the US DOE, BES Office, Division of Materials Sciences and Engineering under award DE-SC0001819 (g-factor analysis by J.M.P.), and the Gordon and Betty Moore Foundation's EPiQS Initiative through grant GBMF4541 to P.J.-H. K.W. and T.T. acknowledge support from the Elemental Strategy Initiative conducted by the MEXT, Japan, A3 Foresight by JSPS and the CREST (JPMJCR15F3), JST. This work made use of the Materials Research Science and Engineering Center Shared Experimental Facilities supported by the National Science Foundation (DMR-0819762) and of Harvard's Center for Nanoscale Systems, supported by the NSF (ECS-0335765). D.R.-L. acknowledges partial support from Fundació Bancaria "la Caixa" (LCF/BQ/AN15/10380011) and from the US Army Research Office grant number W911NF-17-S-0001 (measurements). O.R.-B. acknowledges support from Fundació Privada Cellex.

Author contributions Y.C., D.R.-L., O.R.-B. and J.M.P contributed to sample fabrication and transport measurements. Y.C., D.R.-L., O.R.-B., J.M.P and P.J.-H. performed data analysis. K.W. and T.T. provided h-BN samples. Y.C., D.R.-L., O.R.-B., J.M.P. and P.J.-H. wrote the manuscript with input from all co-authors.

Competing interests The authors declare no competing interests.

Additional information
Correspondence and requests for materials should be addressed to Y.C. or P.J.-H.

Peer review information *Nature* thanks Ming-Hao Liu, Hu-Jong Lee and the other, anonymous, reviewer(s) for their contribution to the peer review of this work.

Reprints and permissions information is available at http://www.nature.com/reprints.

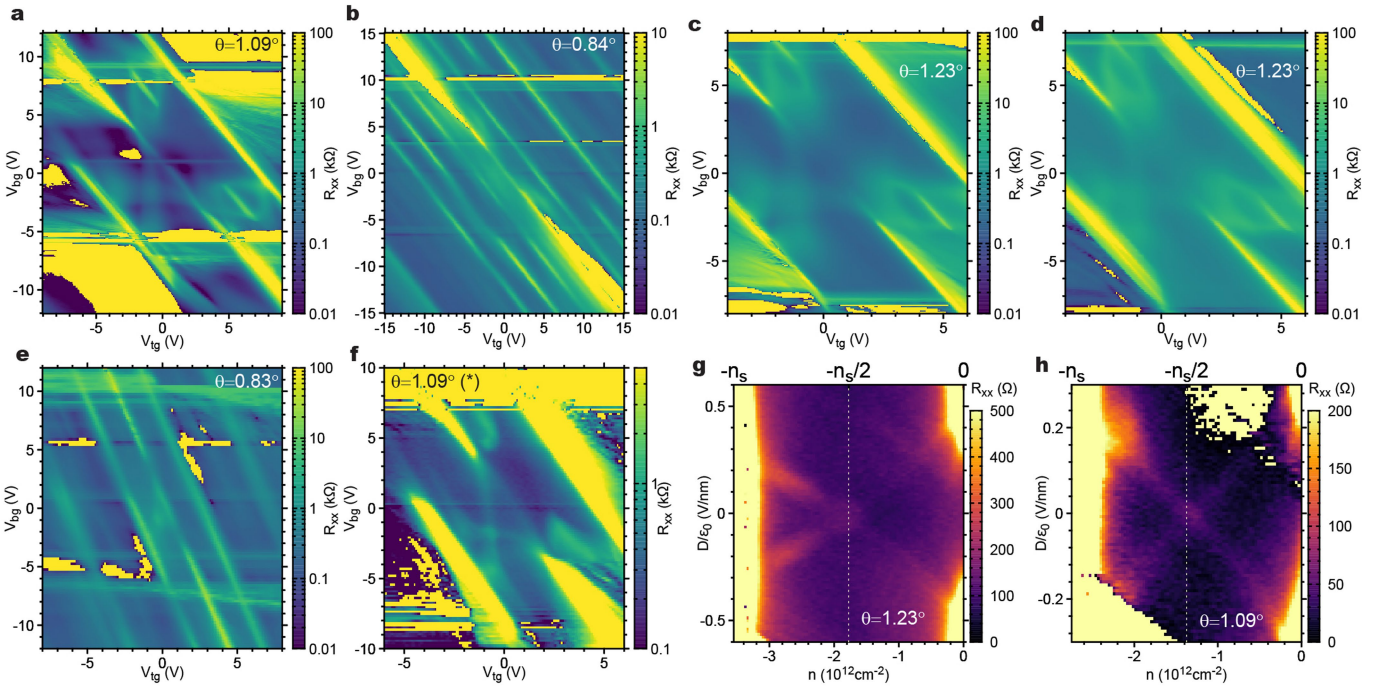

Extended Data Fig. 1 | V_{tg}–V_{bg} resistance maps of measured TBBG devices. **a**–**f**, Resistance versus V_{tg} and V_{bg} for the six TBBG devices measured, which correspond to the six rows shown in Extended Data Table 1, respectively. **g**, **h**, Cross-like feature near $-n_s/2$ in TBBG samples with twist angles $\theta = 1.23°$ (**g**) and $\theta = 1.09°$ (**h**), which might signal the onset of a correlated state.

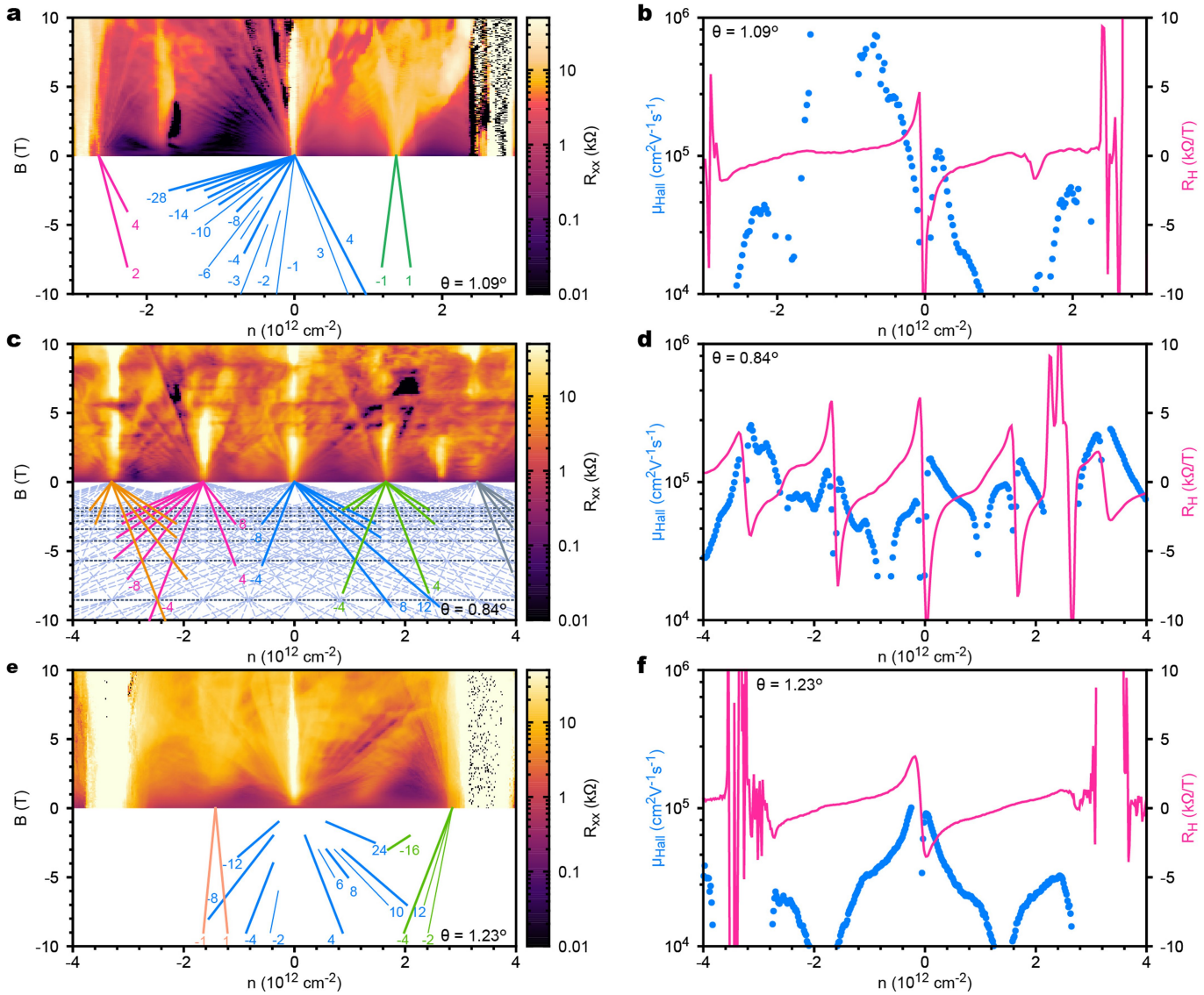

Extended Data Fig. 2 | Landau fan diagrams and Hall mobilities of the TBBG devices. a, Resistance of the 1.09° sample versus carrier density and perpendicular magnetic field. **b**, Hall mobility μ_{Hall} (left axis) and Hall coefficient R_H (right axis) in the 1.09° sample at different carrier densities. **c**–**f**, Same measurements as in **a**, **b** but for the 0.84° (**c**, **d**) and 1.23° (**e**, **f**) samples, respectively. All measurements are taken at $T < 100$ mK. The data for the 1.09° device are taken at $D/\varepsilon_0 = 0.2$ V nm^{-1} while the data for the other two devices are taken at $D = 0$.

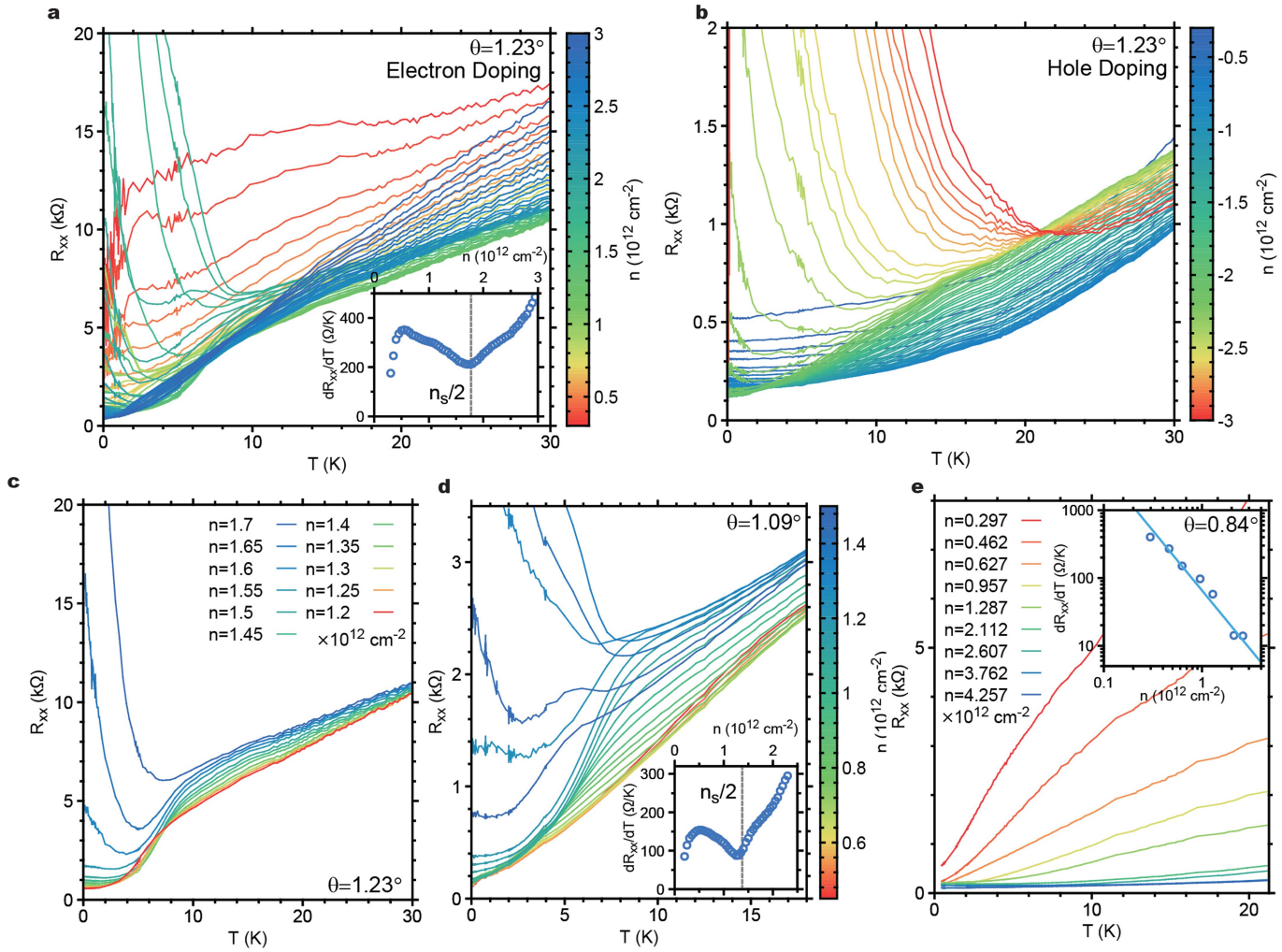

Extended Data Fig. 3 | Linear resistance versus temperature behaviour in TBBG. a, **b**, Resistance versus temperature curves at different charge densities in the 1.23° sample for the electron-doping side (**a**) and the hole-doping side (**b**). The inset in **a** shows the slope dR_{xx}/dT of the linear R–T behaviour as a function of n for T >10 K. **c**, Selected R–T curves near $n_s/2$ from **a**. **d**, Similar linear R–T behaviour in the 1.09° device. The inset shows the slope dR_{xx}/dT. **e**, Density-dependent sublinear/linear R–T behaviour in the 0.84° device. The inset shows the slope dR_{xx}/dT versus n in log–log scale. The slope is proportional to n to the power of −1.77.

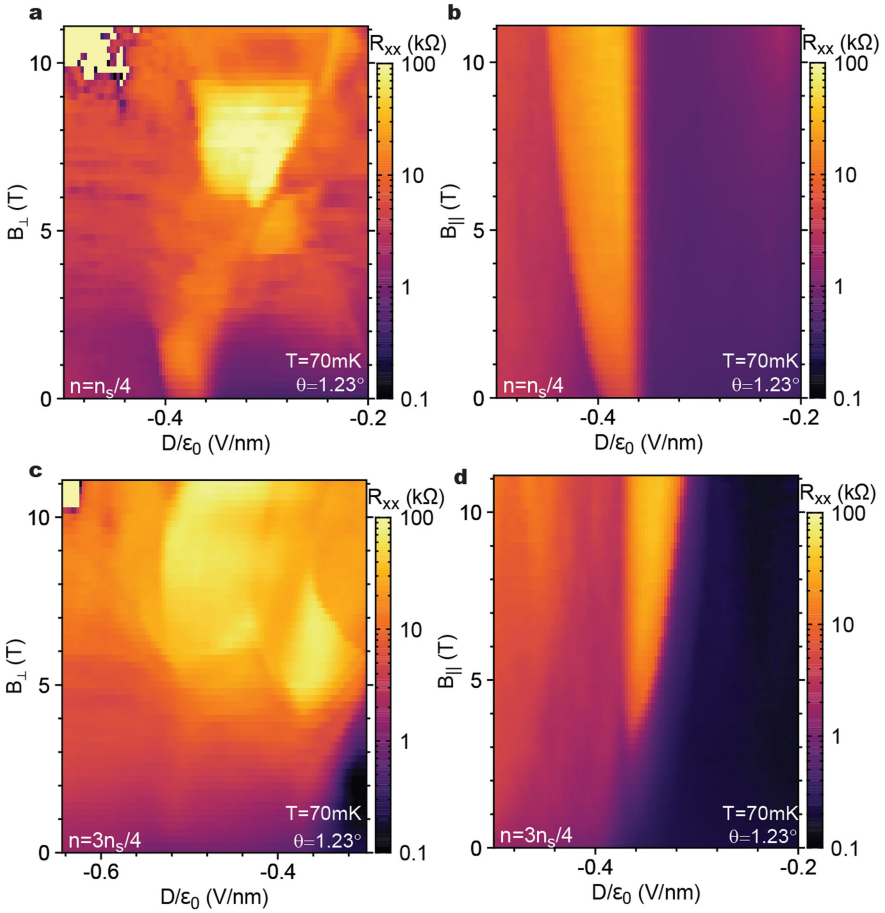

Extended Data Fig. 4 | Additional magnetic field response of TBBG devices. a–d, Response of the $n_s/4$ (**a**, **b**) and $3n_s/4$ (**c**, **d**) states in perpendicular magnetic field (**a**, **c**) and in-plane magnetic field (**b**, **d**) for the θ =1.23° device.

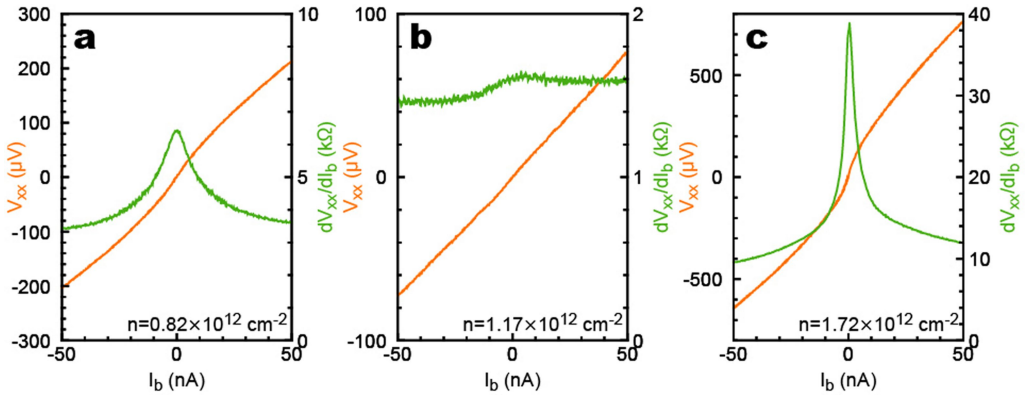

Extended Data Fig. 5 | *I*–*V* curves in the 1.23° TBBG device at different carrier densities. $D/\varepsilon_0 = -0.38\ \mathrm{V\,nm^{-1}}$. **a**–**c**, The densities correspond approximately to the $n_s/4$ (**a**) and $n_s/2$ (**c**) insulating states while the density for **b** lies between them. The left axis is the longitudinal voltage V_{xx} and the right axis is the differential resistance $\mathrm{d}V_{xx}/\mathrm{d}I_b$.

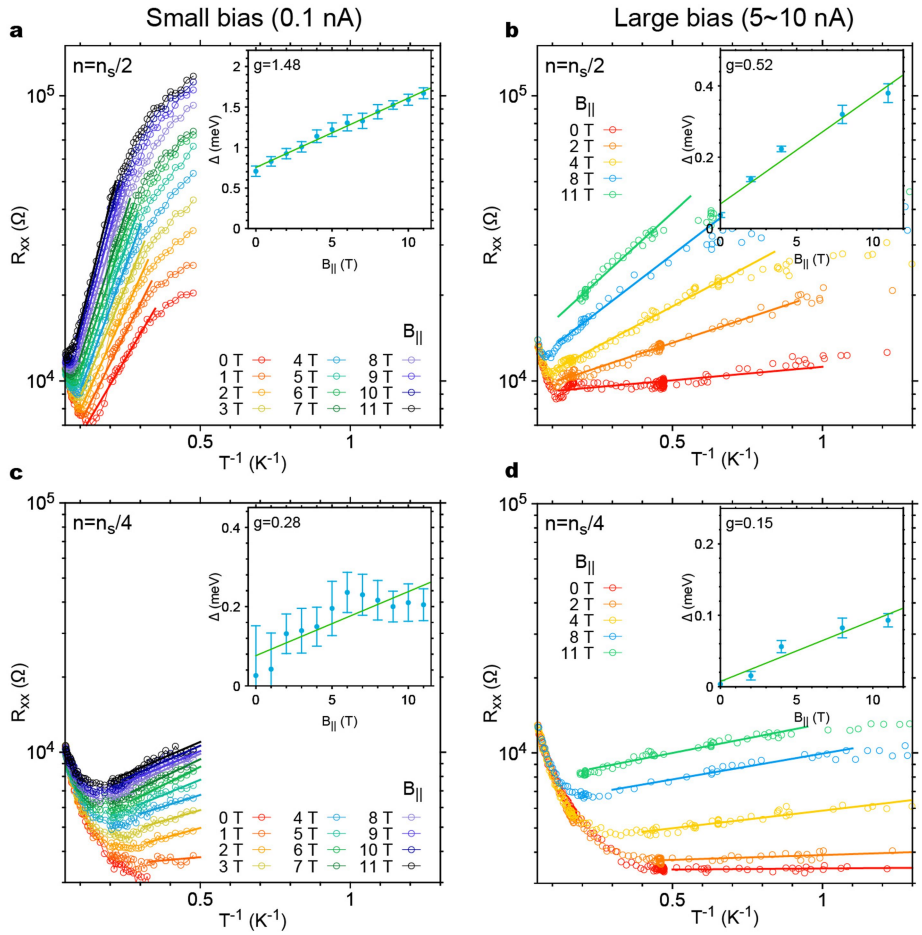

Extended Data Fig. 6 | Comparison of the gap sizes and the g-factor using small and large excitations. a, **b**, The Arrhenius fits of the resistance at the $n_s/2$ state of the 1.23° TBBG device in an in-plane magnetic field. **c**, **d**, The same fits for the $n_s/4$ state. **a** and **c** are measured using a current excitation of 0.1 nA, while **b** and **d** are measured using a voltage excitation of around 100 μV, which induces a current of around 5–10 nA in the sample. The insets in each panel show the corresponding *g*-factor fittings. In general, by using an excessive excitation, both the energy gaps and the *g*-factor will be underestimated.

Extended Data Table 1 | List of TBBG devices discussed in the main text and Extended Data figures

θ(°)	c_{tg}(F/m^2)	c_{bg}(F/m^2)	$V_{tg,0}$(V)	$V_{bg,0}$(V)	n_s(cm^{-2})
1.09	6.63×10^{-4}	5.02×10^{-4}	0.30	0.58	2.75×10^{12}
1.23	1.06×10^{-3}	7.14×10^{-4}	0.41	-0.04	3.55×10^{12}
1.23	1.06×10^{-3}	7.14×10^{-4}	0.41	-0.04	3.55×10^{12}
0.84	6.87×10^{-4}	6.38×10^{-4}	0.06	0.08	1.65×10^{12}
0.79	1.06×10^{-3}	3.57×10^{-4}	0.18	0.67	1.45×10^{12}
1.09(*)	1.03×10^{-3}	5.12×10^{-4}	0.28	0.45	2.75×10^{12}

The last device is marked with an asterisk to differentiate it from the first device, which happens to have the same twist angle, but it is a totally independent device fabricated on a separate chip.